

Electromagnetic induction in non-uniform domains.

A. Giesecke^a, C. Nore^{b,c}, F. Luddens^{b,e}, F. Stefani^a, G. Gerbeth^a, J. Léorat^d, J.-L. Guermond^{b,e}

^a*Forschungszentrum Dresden-Rossendorf, Dresden, Germany*

^b*Laboratoire d'Informatique pour la Mécanique et les Sciences de l'Ingénieur, CNRS, BP 133, 91403 Orsay cedex, France*

^c*Université Paris Sud 11, 91405 Orsay cedex, France et Institut Universitaire de France*

^d*Luth, Observatoire de Paris-Meudon, place Janssen, 92195-Meudon, France*

^e*Department of Mathematics, Texas A&M University 3368 TAMU, College Station, TX 77843, USA*

(Received 00 Month 200x; in final form 00 Month 200x)

Kinematic simulations of the induction equation are carried out for different setups suitable for the von-Kármán-Sodium (VKS) dynamo experiment. Material properties of the flow driving impellers are considered by means of high conducting and high permeability disks that are present in a cylindrical volume filled with a conducting fluid. Two entirely different numerical codes are mutually validated by showing quantitative agreement on Ohmic decay and kinematic dynamo problems using various configurations and physical parameters. Field geometry and growth rates are strongly modified by the material properties of the disks even if the high permeability/high conductivity material is localized within a quite thin region. In contrast the influence of external boundary conditions remains small.

Utilizing a VKS like mean fluid flow and high permeability disks yields a reduction of the critical magnetic Reynolds number for the onset of dynamo action of the simplest non-axisymmetric field mode. However this decrease is not sufficient to become relevant in the VKS experiment. Furthermore, the reduction of Rm^c is essentially influenced by tiny changes in the flow configuration so that the result is not very robust against small modifications of setup and properties of turbulence.

Keywords: Magnetohydrodynamics, Ohmic decay, kinematic Dynamo, Permeability, VKS dynamo

1 Introduction

Magnetic fields of galaxies, stars or planets are produced by homogenous dynamo action in which a conducting fluid flow provides for generation and maintenance of field energy. During the past decade the understanding of the field generation mechanism has considerably benefited from the examination of dynamo action in the laboratory. However, realization of dynamo action at least requires the magnetic Reynolds number $Rm = UL/\eta$ to exceed a threshold of the order of $Rm^{crit} \sim 10 \dots 100$. From the parameter values of liquid sodium – the best known liquid conductor – at standard laboratory conditions (i.e. $T \approx 200^\circ\text{C}$, $\eta = 1/\mu_0\sigma \approx 0.1\text{m}^2/\text{s}$ and $\mathcal{L} \approx 1\text{m}$, where μ_0 is the vacuum permeability and σ the electrical conductivity) it becomes immediately obvious that self excitation of magnetic fields in the laboratory needs typical velocity magnitudes of $U \sim 10\text{m/s}$, which is already quite demanding. Therefore, the first successful dynamo experiments performed by Lowes and Wilkinson (1963, 1968) utilized soft-iron material so that the magnetic diffusivity is reduced and the magnetic Reynolds number is (at least locally) increased. Although these experiments cannot be classified as hydromagnetic dynamos (no fluid flow and therefore no backreaction of the field on a fluid motion) they allowed the examination of distinct dynamical regimes manifested in steady, oscillating or reversing fields. It is interesting to note that these results did not initiate further numerical studies on induction in the presence of soft iron domains.

A possibility to increase the effective magnetic Reynolds number in fluid flow driven dynamo experiments arises from the addition of tiny ferrous particles to the fluid medium leading to an uniform enlargement

*Corresponding author. Email: a.giesecke@fzd.de

of the relative permeability (Frick *et al.* 2002, Dobler *et al.* 2003). To retain reasonable fluid properties the amount of particles added to the liquid is limited so that an upper bound for the achievable fluid permeability is given by $\mu_r \approx 2$. The main effect found in the simulations of Dobler *et al.* (2003) was a reduced decay of the initial field but not a smaller threshold (essentially because of nonmonotonous behavior of the growth rate in dependence of Rm).

Another type of ferromagnetic influence on dynamo action is observed in the von-Kármán-sodium (VKS) dynamo. In the VKS experiment a turbulent flow of liquid sodium is driven by two counterrotating impellers located at the opposite end caps of a cylindrical domain (Monchaux *et al.* 2007). Dynamo action is only obtained when the impellers are made of soft-iron with $\mu_r \sim 100$ (Verhille *et al.* 2010). Recently it has been shown in Giesecke *et al.* (2010b) that these soft-iron impellers essentially determine the geometry and the growth rates of the magnetic field by locally enhancing the magnetic Reynolds number and by enforcing internal boundary conditions for the magnetic field at the material interfaces in terms of jump conditions. Furthermore, gradients of the material coefficients μ_r and σ might support dynamo action because corresponding additional terms in the induction equation couple toroidal and poloidal fields which is essential for the occurrence of dynamo action. An example for this dynamo type has been presented in Busse and Wicht (1992) where it was shown that even a straight flow over an (infinite) conducting plate with sinusoidal variation of the conductivity is able to produce dynamo action. However, the experimental realization of this setup would require either an unachievable large magnetic Reynolds number or a rather large variation in the conductivity (\gtrsim factor of 100) whereas the mean value should not be too far away from the conductivity of the fluid. In order to obtain semi-homogenous dynamo action it might be more promising to replace the conductivity variation by a permeability variation because the relative permeability of soft-iron alloys easily attains values of several thousands. Although such dynamos are of little astrophysical relevance the experiments of Lowes and Wilkinson and in particular the rich dynamical behavior in the VKS dynamo demonstrate the usefulness of such models.

The scope of the present work is to validate the numerical tool necessary to establish a basic understanding of the influence of material properties on the induction process. Emphasis is given to the problem of the free decay in cylindrical geometry where two disks characterized by high conductivity/permeability and their thickness are inserted in the interior of a cylindrical container filled with a conducting fluid. To demonstrate the reliability of our results we use two different numerical approaches and show that both methods give results in agreement. The study is completed by an application of a mean flow as it occurs in the VKS experiment in combination with two high permeability disks.

2 Induction equation in heterogenous domains

From Faraday's Law in combination with Ohm's Law one immediately retrieves the induction equation that determines the temporal behavior of the magnetic flux density \mathbf{B} (often abbreviated with magnetic field):

$$\frac{\partial \mathbf{B}}{\partial t} = \nabla \times \left(\mathbf{u} \times \mathbf{B} - \frac{1}{\mu_0 \sigma} \nabla \times \frac{\mathbf{B}}{\mu_r} \right). \quad (2.1)$$

In Eq. (2.1) \mathbf{u} denotes the flow velocity, σ the electric conductivity, μ_0 the vacuum permeability and μ_r the relative permeability. In case of spatially varying distributions of conductivity and permeability Eq. (2.1) can be rewritten:

$$\begin{aligned} \frac{\partial \mathbf{B}}{\partial t} = & \nabla \times (\mathbf{u} \times \mathbf{B}) + \frac{1}{\mu_0 \mu_r \sigma} \Delta \mathbf{B} + \frac{1}{\mu_0 \mu_r \sigma} \nabla \times (\nabla \ln \mu_r \times \mathbf{B}) \\ & - \frac{1}{\mu_0 \mu_r \sigma} (\nabla \ln \mu_r + \nabla \ln \sigma) \times (\nabla \ln \mu_r \times \mathbf{B}) + \frac{1}{\mu_0 \mu_r \sigma} (\nabla \ln \mu_r + \nabla \ln \sigma) \times (\nabla \times \mathbf{B}) \end{aligned} \quad (2.2)$$

The terms on the right-hand-side that involve gradients of μ_r and σ couple the toroidal and poloidal field components which is known to be essential for the existence of a dynamo. The lack of symmetry between

the terms containing μ_r and σ indicates a distinct impact of σ and μ_r which is also manifested in the jump conditions for electric field and magnetic field that have to be fulfilled at material interfaces. At interfaces between materials 1 and 2 that exhibit a jump in conductivity σ and/or in relative permeability μ_r the normal component of the magnetic flux density is continuous whereas the tangential components exhibit a jump described by the ratio of the permeabilities. In case of conductivity discontinuities, the tangential components of the electric field are continuous and the normal component of the electric current is continuous. If there is no contribution of the flow, the continuity of the normal current leads to the discontinuity of the normal electric field in the ratio of the conductivities. Mathematically these jump conditions are given by (see e.g. Jackson, 1975):

$$\begin{aligned} \mathbf{n} \cdot (\mathbf{B}_1 - \mathbf{B}_2) &= 0, \\ \mathbf{n} \times \left(\frac{\mathbf{B}_1}{\mu_{r,1}} - \frac{\mathbf{B}_2}{\mu_{r,2}} \right) &= 0, \\ \mathbf{n} \cdot (\mathbf{j}_1 - \mathbf{j}_2) &= 0, \\ \mathbf{n} \times (\mathbf{E}_1 - \mathbf{E}_2) &= 0, \end{aligned} \tag{2.3}$$

where \mathbf{n} denotes the unit vector in the normal direction on the interface between materials 1 and 2. Although these transmission conditions are standard, their dynamical consequences in flows at large Rm are largely unknown.

3 Numerical schemes

Two different numerical algorithms and codes are used for the numerical solution of problems involving the kinematic induction equation (2.1). A combined finite volume/boundary element method (FV/BEM) is a grid based approach which provides a flexible scheme that utilizes a local discretization and intrinsically maintains the solenoidal character of the magnetic field.

The second solution method is based on a Spectral/Finite Element approximation technique denoted SFEMaNS for Spectral/Finite Elements for Maxwell and Navier-Stokes equations. Taking advantage of the cylindrical symmetry of the domains, Fourier modes are used in the azimuthal direction and finite elements are used in the meridional plane. For each Fourier mode this leads to independent two-dimensional-problems in the meridian plane.

3.1 Hybrid finite volume/boundary element method

We start with the induction equation in conservative form:

$$\frac{\partial \mathbf{B}}{\partial t} + \nabla \times \mathbf{E} = 0 \tag{3.1}$$

where the electric field \mathbf{E} is given by

$$\mathbf{E} = -\mathbf{u} \times \mathbf{B} + \eta \nabla \times \frac{\mathbf{B}}{\mu_r} \tag{3.2}$$

and $\eta = 1/\mu_0\sigma$ is the magnetic diffusivity. For the sake of simplicity we give a short sketch for the treatment of inhomogeneous conductivity and permeability only in Cartesian coordinates. The scheme can easily be adapted to different (orthogonal) coordinate systems (e.g. cylindrical or spherical coordinate system) making use of generalized coordinates (Stone and Norman 1992a,b).

In the finite volume scheme the grid representation of the magnetic field is given by a staggered collocation of the field components that are interpreted as an approximation of the (cell-)face average:

$$\overline{B}_x^{i-\frac{1}{2},j,k} \approx \frac{1}{\Delta y \Delta z} \int_{\Gamma_{yz}} B_x(x_{i-\frac{1}{2}}, y, z) dy dz \quad (3.3)$$

where the integration domain Γ corresponds to the surface of a single cell-face: $\Gamma_{yz} = [y_{j-\frac{1}{2}}, y_{j+\frac{1}{2}}] \times [z_{k-\frac{1}{2}}, z_{k+\frac{1}{2}}]$ (see Fig. 1). A comparable definition is applied for the electric field that is localized at the

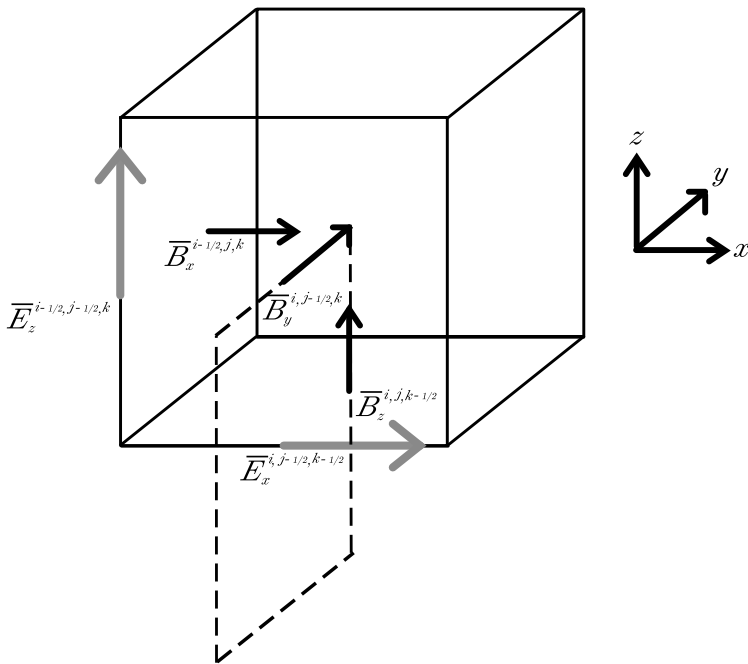


Figure 1. Localization of vector quantities on a grid cell ijk with the cell center located at (x_i, y_j, z_k) . The dotted curve denotes the path along which the integration of \mathbf{B} is executed for the computation of $\overline{E}_x^{i,j-\frac{1}{2},k-\frac{1}{2}}$.

center of a cell edge and which is defined as the line average (see Fig. 1):

$$\overline{E}_x^{i,j-\frac{1}{2},k-\frac{1}{2}} \approx \frac{1}{\Delta x} \int_{x^{i-\frac{1}{2}}}^{x^{i+\frac{1}{2}}} E_x(x, y_{j-\frac{1}{2}}, z_{k-\frac{1}{2}}) dx \quad (3.4)$$

Similar definitions hold for the components $\overline{B}_y^{i,j-\frac{1}{2},k}$ and $\overline{B}_z^{i,j,k-\frac{1}{2}}$, respectively for $\overline{E}_y^{i-\frac{1}{2},j,k-\frac{1}{2}}$ and $\overline{E}_z^{i-\frac{1}{2},j-\frac{1}{2},k}$.

The finite volume discretization of the induction equation reads

$$\frac{d}{dt} \overline{B}_x^{i-\frac{1}{2},j,k} = - \left(\frac{\overline{E}_z^{i-\frac{1}{2},j+\frac{1}{2},k}(t) - \overline{E}_z^{i-\frac{1}{2},j-\frac{1}{2},k}(t)}{\Delta y} - \frac{\overline{E}_y^{i-\frac{1}{2},j,k+\frac{1}{2}}(t) - \overline{E}_y^{i-\frac{1}{2},j,k-\frac{1}{2}}(t)}{\Delta z} \right) \quad (3.5)$$

and it can easily be shown that this approach preserves the $\nabla \cdot \mathbf{B}$ constraint for all times (to machine accuracy) if the initial field is divergence free.

3.1.1 Material coefficients. In the following we only discuss the treatment of the diffusive part of the electric field, $\mathbf{E} = +\eta\nabla \times \mathbf{B}/\mu_r$ because the advective contributions ($\propto -\mathbf{u} \times \mathbf{B}$) do not involve the material properties and can be treated separately in the framework of an operator splitting scheme (see e.g. Iskakov *et al.* 2004, Giesecke *et al.* 2008, Ziegler 1999). To obtain the computation directive for the electric field the magnetic field has to be integrated along a (closed path) around $\overline{E}_x(y,z)$ at the edge of a grid cell (see dotted curve in Fig. 1).

$$\overline{E}_x \approx \frac{1}{\Gamma} \int_{\Gamma_{yz}} E_x dA = \frac{1}{\Gamma} \int_{\Gamma_{yz}} \eta \left(\nabla \times \frac{\mathbf{B}}{\mu_r} \right) dA \approx \frac{\overline{\eta}}{\Delta y \Delta z} \int_{\partial \Gamma_{yz}} \frac{\mathbf{B}}{\mu_r} dl \quad (3.6)$$

where $\Gamma = \Delta y \Delta z$ is the surface surrounded by the path Γ_{yz} and $\overline{\eta}$ is the average diffusivity ($\eta = (\mu_0 \sigma)^{-1}$) "seen" by the electric field. Unlike vectorial quantities the material coefficients are scalar quantities that are localized in the center of a grid cell. The consideration of spatial variations and/or jumps in conductivity respectively permeability is straightforward if corresponding averaging procedures for σ or μ_r are applied (Haber and Ascher 2001). For the component \overline{E}_x the discretization of Eq. (3.6) leads to:

$$\overline{E}_x^{i,j-\frac{1}{2},k-\frac{1}{2}} = \overline{\eta}_{i,j-\frac{1}{2},k-\frac{1}{2}} \left[\frac{1}{\Delta y} \left(\frac{\overline{B}_z^{i,j,k-\frac{1}{2}}}{(\overline{\mu}_r)_{i,j,k-\frac{1}{2}}} - \frac{\overline{B}_z^{i,j-1,k-\frac{1}{2}}}{(\overline{\mu}_r)_{i,j-1,k-\frac{1}{2}}} \right) - \frac{1}{\Delta z} \left(\frac{\overline{B}_y^{i,j-\frac{1}{2},k}}{(\overline{\mu}_r)_{i,j-\frac{1}{2},k}} - \frac{\overline{B}_y^{i,j-\frac{1}{2},k-1}}{(\overline{\mu}_r)_{i,j-\frac{1}{2},k-1}} \right) \right]. \quad (3.7)$$

In Eq. (3.7), $\overline{\eta}_{i,j-\frac{1}{2},k-\frac{1}{2}}$ represents the diffusivity that is seen by the electric field component $\overline{E}_x^{i,j-\frac{1}{2},k-\frac{1}{2}}$ at the edge of the grid cell (ijk) and which is given by the arithmetic average of the diffusivity of the four adjacent cells:

$$\overline{\eta}_{i,j-\frac{1}{2},k-\frac{1}{2}} = \frac{\eta_{i,j,k} + \eta_{i,j-1,k} + \eta_{i-1,j,k} + \eta_{i-1,j-1,k}}{4}. \quad (3.8)$$

Similarly, $\overline{\mu}_r$ denotes the relative permeability that is seen by the magnetic field components (\overline{B}_y and \overline{B}_z) at the interface between two adjacent grid cells which for example reads for the case given in Eq. (3.7):

$$\begin{aligned} \text{for } \overline{B}_y^{i,j-\frac{1}{2},k}: \quad (\overline{\mu}_r)_{i,j-\frac{1}{2},k} &= \frac{2(\mu_r)_{i,j,k}(\mu_r)_{i,j-1,k}}{(\mu_r)_{i,j,k} + (\mu_r)_{i,j-1,k}}, \\ \text{for } \overline{B}_z^{i,j,k-\frac{1}{2}}: \quad (\overline{\mu}_r)_{i,j,k-\frac{1}{2}} &= \frac{2(\mu_r)_{i,j,k}(\mu_r)_{i,j,k-1}}{(\mu_r)_{i,j,k} + (\mu_r)_{i,j,k-1}}. \end{aligned} \quad (3.9)$$

For the computation of $\overline{E}_y^{i-\frac{1}{2},j,k-\frac{1}{2}}$ and $\overline{E}_z^{i-\frac{1}{2},j-\frac{1}{2},k}$ Eq. (3.8) and Eq. (3.9) have to be adjusted according to the localization and the involved field components. Applying the averaging rules (3.8) and (3.9) for the computation of the "diffusive" part of the electric field results in a scheme that intrinsically fulfills the jump conditions (2.3) at material interfaces. The scheme is robust and simple to implement, however, the averaging procedure results in a artificial smoothing of parameter jumps at interfaces and in concave corners additional difficulties might occur caused by ambiguous expressions for μ_r . Furthermore in the simple realization as presented above, the parameter range is restricted. For larger jumps of μ_r or σ a more careful treatment of the discontinuities at the material interfaces is necessary which would require a more elaborate field reconstruction that makes use of slope limiters.

3.1.2 Boundary conditions. In numerical simulations of laboratory dynamo action insulating boundary conditions are often treated adopting simplified expressions like vanishing tangential fields (VTF, sometimes also called pseudo vacuum condition). This ambiguous denomination may be understood only for convecting flows at small magnetic Reynolds number where the induced fields remain small compared to a given field. In fact, a restriction of the boundary magnetic field to its normal component resembles an

artificial but numerically convenient setup where the exterior of the computational domain is characterized by an infinite permeability. In case of VTF boundary conditions the calculation of field growth rates for typical dynamo problems are overestimated. Therefore a more elaborate treatment of the field behavior on the boundary is recommended which is nontrivial in non-spherical coordinate systems. Insulating domains are characterized by a vanishing current $\mathbf{j} \propto \nabla \times \mathbf{B} = 0$ so that \mathbf{B} can be expressed as the gradient of a scalar field Φ (in the case of a simply connected vacuum) which fulfills the Laplace equation:

$$\mathbf{B} = -\nabla\Phi \quad \text{with} \quad \Delta\Phi = 0, \quad \Phi \rightarrow O(r^{-2}) \text{ for } r \rightarrow \infty. \quad (3.10)$$

Integrating $\Delta\Phi = 0$ and adoption of Green's 2nd theorem leads to

$$\Phi(\mathbf{r}) = 2 \int_{\Gamma} G(\mathbf{r}, \mathbf{r}') \underbrace{\frac{\partial\Phi(\mathbf{r}')}{\partial n}}_{-B^n(\mathbf{r}')} - \Phi(\mathbf{r}') \frac{\partial G(\mathbf{r}, \mathbf{r}')}{\partial n} d\Gamma(\mathbf{r}'). \quad (3.11)$$

where $G(\mathbf{r}, \mathbf{r}') = -(4\pi|\mathbf{r} - \mathbf{r}'|)^{-1}$ is the Greens function (with $\Delta G(\mathbf{r}, \mathbf{r}') = -\delta(\mathbf{r} - \mathbf{r}')$) and $\partial/\partial n$ represents the derivative in the normal direction on the surface element $d\Gamma$ so that $\partial_n\Phi = -B^n$ yields the normal component of \mathbf{B} on $d\Gamma$. From Eq. (3.11) the tangential components of the magnetic field on the boundary $B^\tau = \mathbf{e}_\tau \cdot \mathbf{B} = -\mathbf{e}_\tau \cdot \nabla\Phi(\mathbf{r})$ are computed by:

$$B^\tau = 2 \int_{\Gamma} \mathbf{e}_\tau \cdot \left(\Phi(\mathbf{r}') \nabla_r \frac{\partial G(\mathbf{r}, \mathbf{r}')}{\partial n} + B^n(\mathbf{r}') \nabla_r G(\mathbf{r}, \mathbf{r}') \right) d\Gamma(\mathbf{r}') \quad (3.12)$$

where \mathbf{e}_τ represents the tangential unit vector on the surface element $d\Gamma(\mathbf{r}')$. After the subdivision of the surface Γ in boundary elements Γ_j with $\Gamma = \cup \Gamma_j$ the potential $\Phi_i = \Phi(\mathbf{r}_i)$ and the tangential field $B_i^\tau = B^\tau(\mathbf{r}_i) = -\mathbf{e}_\tau \cdot (\nabla\Phi_i)$ in discretized form are given by

$$\begin{aligned} \frac{1}{2}\Phi_i &= - \sum_j \left(\int_{\Gamma_j} \frac{\partial G}{\partial n}(\mathbf{r}_i, \mathbf{r}') d\Gamma'_j \right) \Phi_j, - \sum_j \left(\int_{\Gamma_j} G(\mathbf{r}_i, \mathbf{r}') d\Gamma'_j \right) B_j^n \\ B_i^\tau &= \sum_j \left(\int_{\Gamma_j} 2\mathbf{e}_\tau \cdot \nabla_r \frac{\partial G}{\partial n}(\mathbf{r}_i, \mathbf{r}') d\Gamma'_j \right) \Phi_j + \sum_j \left(\int_{\Gamma_j} 2\mathbf{e}_\tau \cdot \nabla_r G(\mathbf{r}_i, \mathbf{r}') d\Gamma'_j \right) B_j^n. \end{aligned} \quad (3.13)$$

The solution of the system of equations (3.13) gives a linear, non local relation for the tangential field components on the boundary in terms of the normal components and closes the problem of magnetic induction in finite (connected) domains with insulating boundaries (Iskakov and Dormy 2005). A more detailed description of the scheme can be found in Giesecke *et al.* (2008).

3.2 Spectral/Finite Elements for Maxwell equations

The conducting part of the computational domain is denoted Ω_c , the non-conducting part (vacuum) is denoted Ω_v , and we set $\Omega := \Omega_c \cup \Omega_v$. We use the subscript c for the conducting part and v for the vacuum. We assume that Ω_c is partitioned into subregions $\Omega_{c1}, \dots, \Omega_{cN}$, so that the magnetic permeability in each subregion Ω_{ci} , say μ^{ci} , is smooth. We denote Σ_μ the interface between all the conducting subregions. We denote Σ the interface between Ω_c and Ω_v .

The electric and magnetic fields in Ω_c and Ω_v solve the following system:

$$\frac{\partial(\mu^c \mathbf{H}^c)}{\partial t} = -\nabla \times \mathbf{E}^c, \quad \frac{\partial(\mu^v \mathbf{H}^v)}{\partial t} = -\nabla \times \mathbf{E}^v, \quad (3.14)$$

$$\nabla \cdot \mu^c \mathbf{H}^c = 0, \quad \nabla \cdot \mu^v \mathbf{H}^v = 0, \quad (3.15)$$

$$\mathbf{E}^c = -\mathbf{u} \times \mu^c \mathbf{H}^c + \frac{1}{\sigma} \nabla \times \mathbf{H}^c, \quad \nabla \times \mathbf{H}^v = 0. \quad (3.16)$$

and the following transmission conditions hold across Σ_μ and Σ :

$$\mathbf{H}^{ci} \times \mathbf{n}^{ci} + \mathbf{H}^{cj} \times \mathbf{n}^{cj} = 0, \quad \mathbf{H}^c \times \mathbf{n}^c + \mathbf{H}^v \times \mathbf{n}^v = 0, \quad (3.17)$$

$$\mu^{ci} \mathbf{H}^{ci} \cdot \mathbf{n}^c + \mu^{cj} \mathbf{H}^{cj} \cdot \mathbf{n}^{cj} = 0, \quad \mu^c \mathbf{H}^c \cdot \mathbf{n}^c + \mu^v \mathbf{H}^v \cdot \mathbf{n}^v = 0 \quad (3.18)$$

$$\mathbf{E}^{ci} \times \mathbf{n}^{ci} + \mathbf{E}^{cj} \times \mathbf{n}^{cj} = 0, \quad \mathbf{E}^c \times \mathbf{n}^c + \mathbf{E}^v \times \mathbf{n}^v = 0, \quad (3.19)$$

where \mathbf{n}^c (resp. \mathbf{n}^v) is the outward unit normal on $\partial\Omega_c \cap \Sigma$ (resp. $\partial\Omega_v \cap \Sigma$), and \mathbf{n}^{ci} is the unit outward normal on $\partial\Omega_{ci} \cap \Sigma_\mu$.

3.2.1 Weak formulation. The finite element solution is computed by solving a weak form of the system (3.14)-(3.19). We proceed as follows in Ω_{ci} . Multiplying the induction equation in Ω_{ci} by a test-function \mathbf{b} , integrating over Ω_{ci} and integrating by parts gives

$$\begin{aligned} 0 &= \int_{\Omega_{ci}} \frac{\partial(\mu^{ci} \mathbf{H}^{ci})}{\partial t} \cdot \mathbf{b} + \int_{\Omega_{ci}} \nabla \times \mathbf{E}^{ci} \cdot \mathbf{b} \\ &= \int_{\Omega_{ci}} \frac{\partial(\mu^{ci} \mathbf{H}^{ci})}{\partial t} \cdot \mathbf{b} + \int_{\Omega_{ci}} \mathbf{E}^{ci} \cdot \nabla \times \mathbf{b} + \int_{\partial\Omega_{ci}} (\mathbf{n}^{ci} \times \mathbf{E}^{ci}) \cdot \mathbf{b} \\ &= \int_{\Omega_{ci}} \frac{\partial(\mu^{ci} \mathbf{H}^{ci})}{\partial t} \cdot \mathbf{b} + \int_{\Omega_{ci}} \left(-\mathbf{u} \times \mu^{ci} \mathbf{H}^{ci} + \frac{1}{\sigma} \nabla \times \mathbf{H}^{ci} \right) \cdot \nabla \times \mathbf{b} + \int_{\partial\Omega_{ci}} \mathbf{E}^{ci} \cdot (\mathbf{b} \times \mathbf{n}^{ci}) \end{aligned} \quad (3.20)$$

We proceed slightly differently in Ω_v . From (3.16) we infer that \mathbf{H}^v is a gradient for a simply connected vacuum, i.e., $\mathbf{H}^v = \nabla\phi^v$. Thus taking a test-function of the form $\nabla\psi$, where ψ is a scalar potential defined on Ω_v , multiplying (3.14) by $\nabla\psi$ and integrating over Ω_v , we obtain

$$\int_{\Omega_v} \frac{\partial(\mu^v \nabla\phi^v)}{\partial t} \cdot \nabla\psi + \int_{\Sigma} \mathbf{E}^v \cdot \nabla\psi \times \mathbf{n}^v + \int_{\partial\Omega} \mathbf{E}^v \cdot \nabla\psi \times \mathbf{n}^v = 0 \quad (3.21)$$

We henceforth assume that $\mathbf{a} := \mathbf{E}|_{\partial\Omega}$ is a data. Since only the tangential parts of the electric field are involved in the surface integrals in (3.20) and (3.21), we can use the jump conditions (3.19) to write

$$\int_{\Sigma_\mu} \mathbf{E}^{ci} \cdot \mathbf{b} \times \mathbf{n}^{ci} = \int_{\Sigma_\mu} \{\mathbf{E}^c\} \cdot \mathbf{b} \times \mathbf{n}^{ci}, \quad \int_{\Sigma} \mathbf{E}^v \cdot \nabla\psi \times \mathbf{n}^v = \int_{\Sigma} \mathbf{E}^c \cdot \nabla\psi \times \mathbf{n}^v,$$

where $\{\mathbf{E}^c\}$ is defined on Σ_μ by $\{\mathbf{E}^c\} = \frac{1}{2}(\mathbf{E}^{ci} + \mathbf{E}^{cj})$. We now add (3.20) (for $i = 1, \dots, N$) and (3.21)

to obtain

$$\begin{aligned} \int_{\Omega_c} \frac{\partial(\mu^c \mathbf{H}^c)}{\partial t} \cdot \mathbf{b} + \int_{\Omega_v} \frac{\partial(\mu^v \nabla \phi^v)}{\partial t} \cdot \nabla \psi + \int_{\cup_{i=1}^N \Omega_{ci}} \left(\frac{1}{\sigma} \nabla \times \mathbf{H}^{ci} - \mathbf{u} \times \mu^{ci} \mathbf{H}^{ci} \right) \cdot \nabla \times \mathbf{b} \\ + \int_{\Sigma_\mu} \{ \mathbf{E}^c \} \cdot [\mathbf{b} \times \mathbf{n}] + \int_{\Sigma} \mathbf{E}^c \cdot (\mathbf{b} \times \mathbf{n}^c + \nabla \psi \times \mathbf{n}^v) = - \int_{\partial \Omega} \mathbf{a} \cdot \nabla \psi \times \mathbf{n}^v, \end{aligned}$$

where we have set $[\mathbf{b} \times \mathbf{n}] := (\mathbf{b}_i \times \mathbf{n}^{ci} + \mathbf{b}_j \times \mathbf{n}^{cj})$ with $\mathbf{b}_i := \mathbf{b}|_{\Omega_{ci}}$ and $\mathbf{b}_j := \mathbf{b}|_{\Omega_{cj}}$. We finally get rid of \mathbf{E}^c by using Ohm's law in the conductor:

$$\begin{aligned} \int_{\Omega_c} \frac{\partial(\mu^c \mathbf{H}^c)}{\partial t} \cdot \mathbf{b} + \int_{\Omega_v} \frac{\partial(\mu^v \nabla \phi^v)}{\partial t} \cdot \nabla \psi + \int_{\cup_{i=1}^N \Omega_{ci}} \left(\frac{1}{\sigma} \nabla \times \mathbf{H}^{ci} - \mathbf{u} \times \mu^{ci} \mathbf{H}^{ci} \right) \cdot \nabla \times \mathbf{b} \\ + \int_{\Sigma_\mu} \left\{ \frac{1}{\sigma} \nabla \times \mathbf{H}^c - \mathbf{u} \times \mu^c \mathbf{H}^c \right\} \cdot [\mathbf{b} \times \mathbf{n}] + \int_{\Sigma} \left(\frac{1}{\sigma} \nabla \times \mathbf{H}^c - \mathbf{u} \times \mu^c \mathbf{H}^c \right) \cdot (\mathbf{b} \times \mathbf{n}^c + \nabla \psi \times \mathbf{n}^v) = - \int_{\partial \Omega} \mathbf{a} \cdot \nabla \psi \times \mathbf{n}^v \end{aligned} \quad (3.22)$$

This formulation is the starting point for the finite element discretization.

3.2.2 Space discretization. As already mentioned, SFEMaNS takes advantage of the cylindrical symmetry. We denote Ω_v^{2d} and Ω_{ci}^{2d} the meridian sections of Ω_v and Ω_{ci} , respectively. These sections are meshed using quadratic triangular meshes (we assume that Ω_v^{2d} and the sub-domains $\Omega_{c1}^{2d} \dots \Omega_{cN}^{2d}$ have piecewise quadratic boundaries). We denote $\{\mathcal{F}_h^v\}_{h>0}$, $\{\mathcal{F}_h^{c1}\}_{h>0} \dots \{\mathcal{F}_h^{cN}\}_{h>0}$ the corresponding regular families of non-overlapping quadratic triangular meshes. For every K in the mesh we denote $T_K : \hat{K} \rightarrow K$ the quadratic transformation that maps the reference triangle $\hat{K} := \{(\hat{r}, \hat{z}) \in \mathbb{R}^2, 0 \leq \hat{r}, 0 \leq \hat{z}, \hat{r} + \hat{z} \leq 1\}$ to K . Given ℓ_H and ℓ_ϕ two integers in $\{1, 2\}$ with $\ell_\phi \geq \ell_H$ we first define the meridian finite elements spaces

$$\begin{aligned} \mathbf{X}_h^{H,2d} &:= \{ \mathbf{b}_h \in \mathbf{L}^1(\Omega_c) / \mathbf{b}_h|_{\Omega_{ci}} \in \mathcal{C}^0(\overline{\Omega_{ci}}), \forall i = 1, \dots, M, \mathbf{b}_h(T_K) \in \mathbb{P}_{\ell_H}, \forall K \in \cup_{i=1}^N \mathcal{F}_h^{ci} \}, \\ X_h^{\phi,2d} &:= \{ \psi_h \in \mathcal{C}^0(\overline{\Omega_v}) / \psi_h(T_K) \in \mathbb{P}_{\ell_\phi}, \forall K \in \mathcal{F}_h^v \}, \end{aligned}$$

where \mathbb{P}_k denotes the set of (scalar or vector valued) bivariate polynomials of total degree at most k . Then, using the complex notation $i^2 = -1$, the magnetic field and the scalar potential are approximated in the following spaces:

$$\begin{aligned} \mathbf{X}_h^H &:= \left\{ \mathbf{b}_h = \sum_{m=-M}^M \mathbf{b}_h^m(r, z) e^{im\theta}; \forall m = 0, \dots, M, \mathbf{b}_h^m \in \mathbf{X}_h^{H,2d} \text{ and } \mathbf{b}_h^m = \overline{\mathbf{b}_h^{-m}} \right\}, \\ X_h^\phi &:= \left\{ \psi_h = \sum_{m=-M}^M \psi_h^m(r, z) e^{im\theta}; \forall m = 0, \dots, M, \psi_h^m \in X_h^{\phi,2d} \text{ and } \psi_h^m = \overline{\psi_h^{-m}} \right\}, \end{aligned}$$

where $M + 1$ is the maximum number of complex Fourier modes.

3.2.3 Time discretization. We approximate the time derivatives using the second-order Backward Difference Formula (BDF2). The terms that are likely to mix Fourier modes are made explicit. Let Δt be the time step and set $t^n := n\Delta t$, $n \geq 0$. After proper initialization at t^0 and t^1 , the algorithm proceeds as

follows. For $n \geq 1$ we set

$$\mathbf{H}^* = 2\mathbf{H}^{c,n} - \mathbf{H}^{c,n-1}, \quad \text{and} \quad \begin{cases} D\mathbf{H}^{c,n+1} := \frac{1}{2} (3\mathbf{H}^{c,n+1} - 4\mathbf{H}^{c,n} + \mathbf{H}^{c,n-1}) \\ D\phi^{v,n+1} := \frac{1}{2} (3\phi^{v,n+1} - 4\phi^{v,n} + \phi^{v,n-1}), \end{cases}$$

and the discrete fields $\mathbf{H}^{c,n+1} \in \mathbf{X}_h^H$ and $\phi^{v,n+1} \in X_h^\phi$ are computed so that the following holds for all $\mathbf{b} \in \mathbf{X}_h^H$, $\psi \in X_h^\phi$:

$$\mathcal{L}((\mathbf{H}^{c,n+1}, \phi^{v,n+1}), (\mathbf{b}, \psi)) = \mathcal{R}(\mathbf{b}, \psi), \quad (3.23)$$

where the linear for \mathcal{R} is defined by

$$\mathcal{R}(\mathbf{b}, \psi) = - \int_{\partial\Omega} \mathbf{a} \cdot \nabla \psi \times \mathbf{n}^v + \int_{\Omega_c} \mathbf{u} \times \mu^c \mathbf{H}^* \cdot \nabla \times \mathbf{b} + \int_{\Sigma_\mu} \{\mathbf{u} \times \mu^c \mathbf{H}^*\} \cdot \llbracket \mathbf{b} \times \mathbf{n} \rrbracket + \int_{\Sigma} \mathbf{u} \times \mu^c \mathbf{H}^* \cdot (\mathbf{b} \times \mathbf{n}^c + \nabla \psi \times \mathbf{n}^v),$$

the bilinear form \mathcal{L} is defined by

$$\begin{aligned} \mathcal{L}((\mathbf{H}^{c,n+1}, \phi^{v,n+1}), (\mathbf{b}, \psi)) &:= \int_{\Omega_c} \mu^c \frac{D\mathbf{H}^{c,n+1}}{\Delta t} \cdot \mathbf{b} + \int_{\Omega_v} \mu^v \frac{\nabla D\phi^{v,n+1}}{\Delta t} \cdot \nabla \psi + \int_{\Omega_c} \frac{1}{\sigma} \nabla \times \mathbf{H}^{c,n+1} \cdot \nabla \times \mathbf{b} \\ &+ g((\mathbf{H}^{c,n+1}, \phi^{v,n+1}), (\mathbf{b}, \psi)) + \int_{\Sigma_\mu} \left\{ \frac{1}{\sigma} \nabla \times \mathbf{H}^{c,n+1} \right\} \cdot \llbracket \mathbf{b} \times \mathbf{n} \rrbracket + \int_{\Sigma} \frac{1}{\sigma} \nabla \times \mathbf{H}^{c,n+1} \cdot (\mathbf{b} \times \mathbf{n}^c + \nabla \psi \times \mathbf{n}^v), \end{aligned}$$

and the bilinear form g is defined by

$$\begin{aligned} g((\mathbf{H}_h, \psi_h), (\mathbf{b}_h, \psi_h)) &:= \beta_1 h_F^{-1} \int_{\Sigma_\mu} (\mathbf{H}_{h,1} \times \mathbf{n}_1^c + \mathbf{H}_{h,2} \times \mathbf{n}_2^c) \cdot (\mathbf{b}_{h,1} \times \mathbf{n}_1^c + \mathbf{b}_{h,2} \times \mathbf{n}_2^c) \\ &+ \beta_2 h_F^{-1} \int_{\Sigma} (\mathbf{H}_h \times \mathbf{n}^c + \nabla \psi_h \times \mathbf{n}^v) \cdot (\mathbf{b}_h \times \mathbf{n}^c + \nabla \psi_h \times \mathbf{n}^v), \end{aligned}$$

where h_F denotes the typical size of $\partial K \cup \Sigma_\mu$ or $\partial K \cup \Sigma$ for all K in the mesh such that $\partial K \cup \Sigma_\mu$ or $\partial K \cup \Sigma$ is not empty. The constant coefficients β_1 and β_2 are chosen to be of order 1. The purpose of the bilinear form g is to penalize the tangential jumps $\llbracket \mathbf{H}^{c,n+1} \times \mathbf{n} \rrbracket$ and $\mathbf{H}^{c,n+1} \times \mathbf{n}^c + \nabla \psi^{v,n+1} \times \mathbf{n}^v$, so that they converge to zero when the mesh-size goes to zero.

3.2.4 Addition of a magnetic pressure. The above time-marching algorithm is convergent on finite time intervals but may fail to provide a convergent solution in a steady state regime since errors may accumulate on the divergence of the magnetic induction. We now detail the technique which is employed to control the divergence of \mathbf{B}^c on arbitrary time intervals.

To avoid non-convergence properties that could occur in non-smooth domains and discontinuous material properties, we have designed a non standard technique inspired from Bonito *et al.* (2010) to control $\nabla \cdot \mathbf{B}$. We replace the induction equation in Ω_{ci} , $i = 1, \dots, N$, by the following

$$\frac{\partial(\mu^{ci} \mathbf{H}^{ci})}{\partial t} = -\nabla \times \mathbf{E}^{ci} + \mu^{ci} \nabla p^{ci}, \quad (-\Delta_0)^\alpha p^{ci} = \nabla \cdot \mu^{ci} \mathbf{H}^{ci}, \quad p^{ci}|_{\partial\Omega_{ci}} = 0. \quad (3.24)$$

where α is a real parameter, Δ_0 is the Laplace operator on Ω_{ci} , and p^{ci} is a new scalar unknown. A simple calculation shows that $p^{ci} = 0$ if the initial magnetic induction is solenoidal; hence, (3.24) enforces

$\nabla \cdot \mu^{ci} \mathbf{H}^{ci} = 0$. Taking $\alpha = 0$ amounts to penalizing $\nabla \cdot \mu^{ci} \mathbf{H}^{ci}$ in $L^2(\Omega_{ci})$, which turns out to be non-convergent with Lagrange finite elements when the boundary of Ω_{ci} is not smooth, (see Costabel (1991) for details). The mathematical analysis shows that the method converges with Lagrange finite elements when $\alpha \in (\frac{1}{2}, 1)$. In practice we take $\alpha = 0.7$.

We introduce new finite elements spaces to approximate the new scalar unknown p^c

$$X_h^{p,2d} := \left\{ p_h \in L^1(\Omega_c) / p_h \in C^0(\overline{\Omega_{ci}}), \forall i = 0, \dots, N, p_h(T_K) \in \mathbb{P}_{\ell_p}, \forall K \in \cup_{i=1}^N \mathcal{F}_h^{ci}, p_h = 0 \text{ on } \partial\Omega_{ci} \right\},$$

$$X_h^p := \left\{ p = \sum_{m=-M}^M p^m(r, z) e^{im\theta} / \forall m = 1 \dots, M, p^m \in X_h^{p,2d} \text{ and } p^m = \overline{p^{-m}} \right\}$$

Here ℓ_p is an integer in $\{1, 2\}$. The final form of the algorithm is the following: after proper initialization, we solve for $\mathbf{H}^{c,n+1} \in \mathbf{X}_h^H$, $\phi^{v,n+1} \in X_h^\phi$ and $p^{n+1} \in X_h^p$ so that the following holds for all $\mathbf{b} \in \mathbf{X}_h^H$, $\psi \in X_h^\phi$, $q \in X_h^p$

$$\mathcal{L}((\mathbf{H}^{c,n+1}, \phi^{v,n+1}), (\mathbf{b}, \psi)) + \mathcal{D}((\mathbf{H}^{c,n+1}, p^{c,n+1}, \phi^{v,n+1}), (\mathbf{b}, q, \psi)) + \mathcal{P}(\phi^{v,n+1}, \psi) = \mathcal{R}(\mathbf{b}, \psi) \quad (3.25)$$

with

$$\mathcal{D}((\mathbf{H}, p, \phi), (\mathbf{b}, q, \psi)) := \sum_{i=1}^N \int_{\Omega_{ci}} \left(\mu^c \mathbf{b} \cdot \nabla p - \mu^c \mathbf{H} \cdot \nabla q + h^{2\alpha} \nabla \cdot \mu^c \mathbf{H} \nabla \cdot \mu^c \mathbf{b} + h^{2(1-\alpha)} \nabla p \cdot \nabla q \right) \quad (3.26)$$

where h denotes the typical size of a mesh element. The term $h^{2\alpha} \int_{\Omega_c} \nabla \cdot \mu^c \mathbf{H}^{c,n+1} \nabla \cdot \mu^c \mathbf{b}$ is a stabilization quantity which is added in to have discrete well-posedness of the problem irrespective of the polynomial degree of the approximation for p^c . The additional stabilizing bilinear form \mathcal{P} is defined by

$$\mathcal{P}(\phi, \psi) = \int_{\Omega_v} \nabla \phi \cdot \nabla \psi - \int_{\partial\Omega_v} \psi \mathbf{n} \cdot \nabla \psi.$$

This bilinear form is meant to help ensure that $\Delta \phi^{v,n+1} = 0$ for all times.

3.2.5 Taking advantage from the cylindrical symmetry for Maxwell and Navier-Stokes equations. SFEMaNS is a fully nonlinear code integrating coupled Maxwell and Navier-Stokes equations (Guermond *et al.* (2007, 2009)). As mentioned before, any term that could mix different Fourier modes has been made explicit. Owing to this property, there are $M + 1$ independent linear systems to solve at each time step ($M + 1$ being the maximum number of complex Fourier modes). This immediately provides a parallelization strategy. In practice we use one processor per Fourier mode. The computation of the non-linear terms in right-hand side is done using a parallel Fast Fourier Transform. Note that, in the present paper, we use only the kinematic part of the code with an axisymmetric steady flow. Typical time step is $\Delta t = 0.01$ and typical mesh size is $h = 1/80$ with refined meshes $h = 1/400$ on curved Σ_μ interfaces.

4 Ohmic decay in heterogenous domains

The inspection of equations (2.3) shows that even in the absence of flow, heterogeneous domains can lead to non trivial Ohmic decay problems. Therefore the reliability and the application range of both numerical schemes are first examined by studying pure Ohmic decay problems in absence of flow. A cylindrical geometry is chosen with radius $R = 1.4$ and height $H = 2.6$ which is in accordance with setting of the VKS experiment. The cylinder is filled with a conductor with diffusivity $\eta = (\mu_0 \sigma)^{-1} = 1$ and relative permeability $\mu_r = 1$. Inside the domain two disks are introduced, characterized by thickness d , conductivity

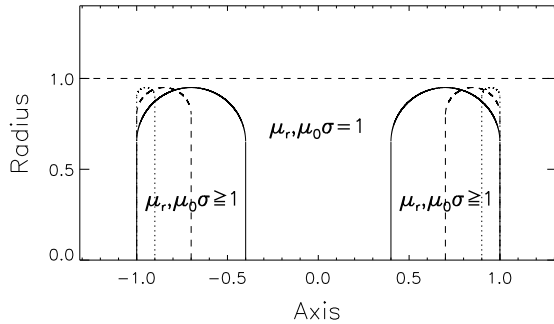


Figure 2. Sketch of the set up. Two disks with thickness $d = 0.6, 0.3, 0.1$ (solid, dashed, dotted curve) are introduced in a cylinder with height $H = 2.6$ and radius $R = 1.4$. In all runs the location of the backside of each disk is fixed at $z = \pm 1$. At the outer disk edge a circular shape is applied with a curvature radius corresponding to half of the disk thickness. The radial extension of the disks is fixed and given by $R_{\text{disk}} = 0.95$. The dashed horizontal line denotes the inner boundary that separates the dynamical active region from the stagnant outer layer in the runs with $\text{Rm} > 0$ (see Sec. 5).

σ and permeability μ_r (see Fig. 2). The thickness $d = 0.1$ is representative of the VKS impellers but the other d have been tested to study the scaling law with an effective permeability or an effective conductivity and also to estimate the impact of the numerical resolutions.

As long as μ_r and σ are axisymmetric, in a freely decaying system the axisymmetric mode ($m = 0$) can be split into decoupled poloidal (B_r, B_z) and toroidal (B_φ) components which decay independently and exhibit two distinct decay rates. The components of azimuthal modes with $m \geq 1$ are coupled and exhibit a single eigenstate and decay rate. In the following we limit our examinations to the decay of the axisymmetric mode ($m = 0$) and the simplest non-axisymmetric mode, the ($m = 1$)-mode ($B \propto \cos \varphi$).

4.1 External boundary conditions and field pattern

A couple of simulations have been performed utilizing vanishing tangential field (VTF) boundary conditions (sometimes also called Pseudo Vacuum) which enforce a field geometry on the outer boundary that resembles the behavior in case of external materials with infinite permeability. Figure 3 shows the structure of the field geometry with the container embedded in vacuum (upper part) and for VTF boundary conditions (lower part). Whereas a significant impact occurs without disks the influence of the external boundary conditions on the field geometry remains negligible if the disk permeability or conductivity is large enough. A more noticeable difference between the field distribution results from the comparison of high permeability disks with high conductive disks. In the first case the field structure is dominated by two distinct annular accumulations of azimuthal magnetic field – essentially located within the disks. The high conducting disk case is characterized by the domination of the axial field with a slab like structure concentrated around the axis in which the high conducting medium is embedded. A remarkable change in the field structure is obtained for the thin disk case ($d = 0.1$, see Fig. 4 & 5). In case of high μ_r the azimuthal field is dominated by two ring like structures centered on the outer part of both disks. The radial field is concentrated within two highly localized paths on the outer edge of the disk whereas the axial field has become nearly independent from z except close to the disks because the jump conditions inhibit the constitution of H_z within the disks. For the high conductive disks, the differences in the field pattern between $d = 0.6$ and $d = 0.1$ are less significant and the torus-like structure of the poloidal field component is always dominating (see right panel in Fig. 5). For increasing permeability, the axisymmetric mode changes from a poloidal dominant structure to a toroidal dominant structure (see Fig. 6 for $d = 0.6$). The mode crossing occurs for $\mu_r^{\text{eff}} \approx 1.5$.

4.2 Decay rates and dominating mode

The temporal behavior of the magnetic eigenmodes follows an exponential law $B \propto e^{\gamma t}$ where γ denotes the growth or decay rate. Figure 7 shows the magnetic field decay rates for a thick disk ($d = 0.6$) and a thin disk ($d = 0.1$) against μ_r^{eff} (left column) and against σ^{eff} (right column) where μ_r^{eff} and σ^{eff} denote effective values for permeability and conductivity that are defined as $\mu_r^{\text{eff}} = V^{-1} \int \mu_r(\mathbf{r}) dV$ and $\sigma^{\text{eff}} = V^{-1} \int \sigma(\mathbf{r}) dV$ with

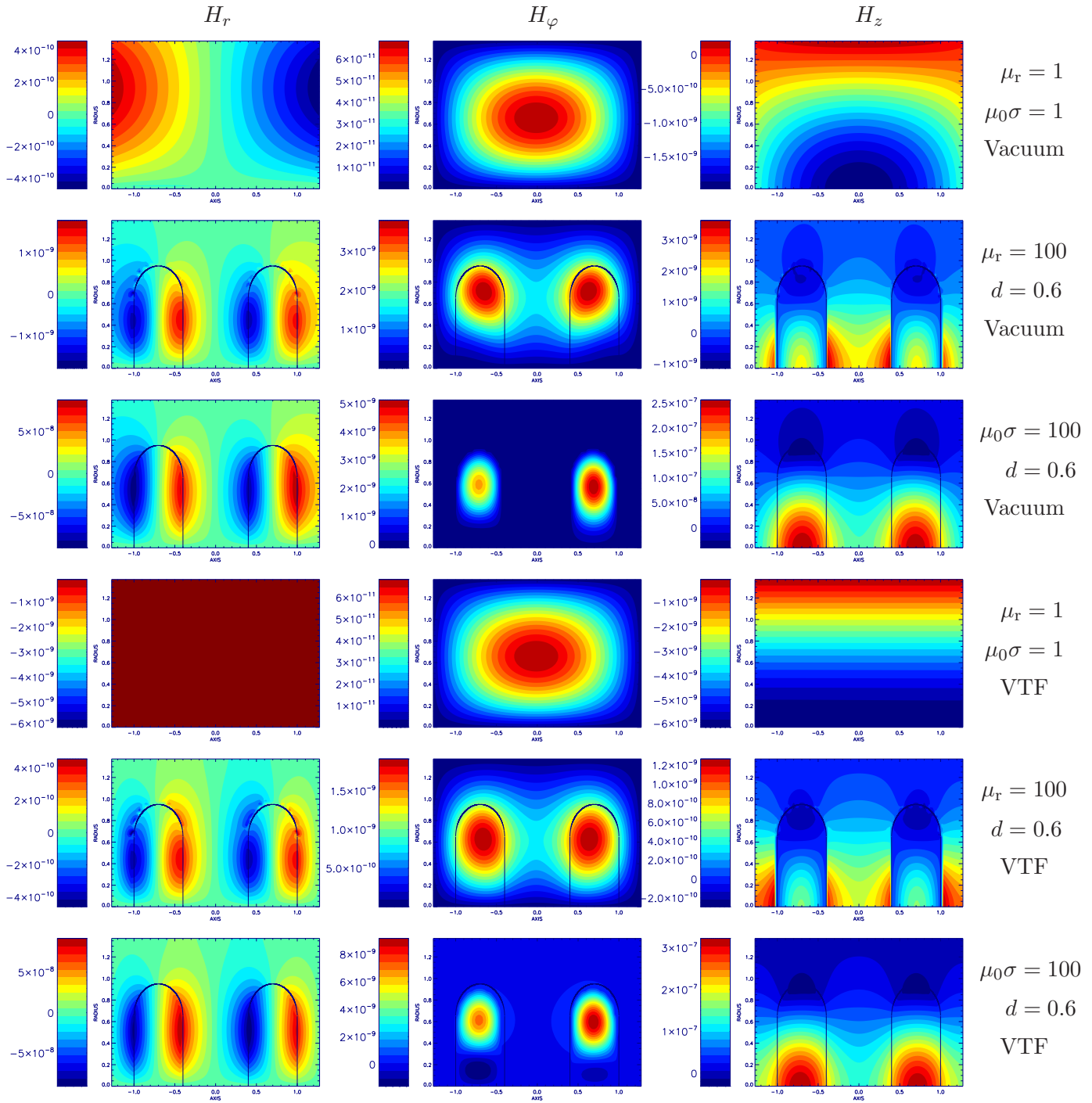


Figure 3. Ohmic decay. Axisymmetric eigenmodes of the magnetic field $\mathbf{H} = \mu_r^{-1} \mathbf{B}$ (from left to right: H_r, H_ϕ, H_z); From top to bottom: $\mu_r = \mu_0 \sigma = 1$ (no disks), $\mu_r = 100, \mu_0 \sigma = 100$ (all with insulating boundary conditions and $d = 0.6$), $\mu_r = \mu_0 \sigma = 1$ (no disks), $\mu_r = 100, \mu_0 \sigma = 100$ (all with vanishing tangential field boundary conditions and $d = 0.6$).

V the volume of the cylindrical domain. The essential properties of the field behavior can be summarized as follows: The presence of high permeability/conductivity material enhances axisymmetric and ($m = 1$) field modes. However, for decreasing thickness the enhancement works selectively for the axisymmetric toroidal field (in case of high μ_r), respectively for the poloidal axisymmetric mode (in case of high σ). For the thin disk the decay rate of the poloidal (respectively toroidal) field component remains nearly independent of the permeability (respectively conductivity). Note the changeover of a dominating axisymmetric poloidal mode to the dominating axisymmetric toroidal mode for the high permeability disks which occurs irrespective of the disk thickness around $\mu_r \approx 1.5$ (see also Fig. 6). The mode crossing does not occur for a high

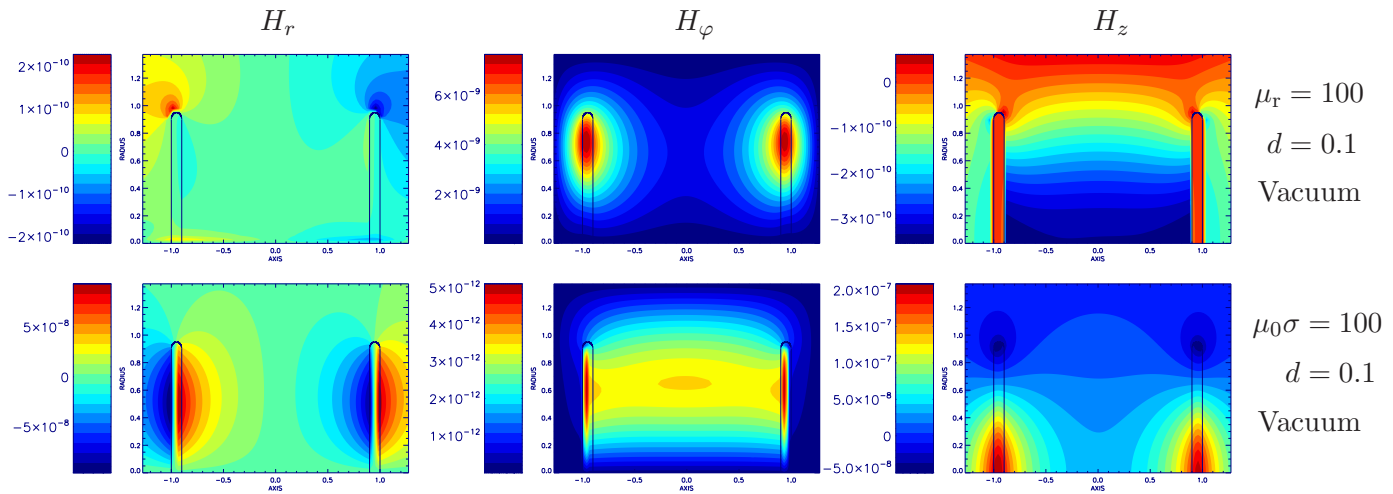


Figure 4. Ohmic decay. Axisymmetric field $\mathbf{H} = \mu_r^{-1} \mathbf{B}$ for the thin disk case ($d = 0.1$, from left to right: H_r, H_φ, H_z); Top row: $\mu_r = 100$, bottom row: $\mu_0 \sigma = 100$. Insulating boundary conditions.

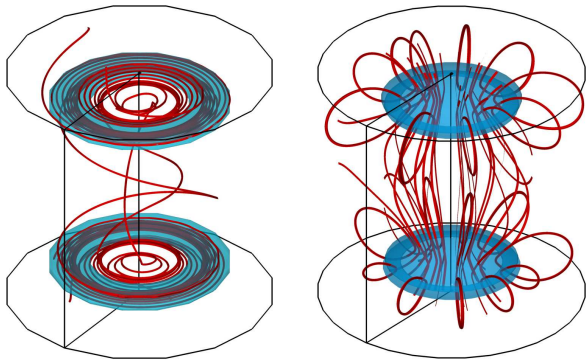


Figure 5. Ohmic decay for thin disks ($d = 0.1$). Left panel: $\mu_r = 100$, right panel: $\mu_0 \sigma = 100$). The isosurfaces present the magnetic energy density at 25% of its maximum value.

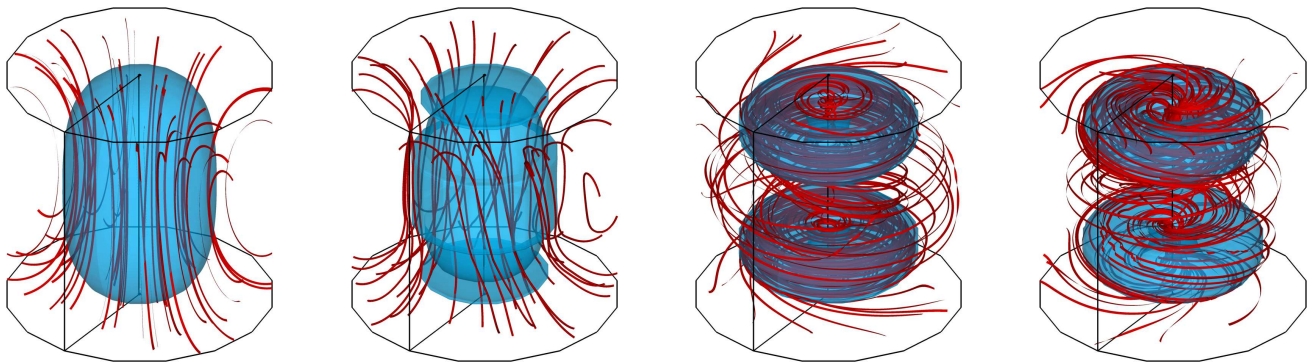


Figure 6. Ohmic decay. The blue transparent isosurfaces present the magnetic energy density at 25% of the maximum value and the red streamlines show the field structure for $d = 0.6$ and (from left to right): $\mu_r = 1, 2, 10, 100$ (corresponding to $\mu_r^{\text{eff}} = 1, 1.2, 2.7, 19.5$).

conducting disk, where the ($m = 1$) mode and the poloidal axisymmetric mode have nearly the same decay rate for $\mu_0 \sigma^{\text{eff}} \lesssim 1.5$ and the axisymmetric poloidal mode dominates for large σ .

Small deviations between both algorithms occur in case of thin disks ($d = 0.1$) for the axisymmetric poloidal mode and for the ($m = 1$) mode. A couple of simulations with higher resolution in axial direction (marked by the blue and the green stars in the lower right panel of Fig. 7) show that these deviations are most probably the result of poor resolution in case of the FV/BEM scheme because only few grid cells

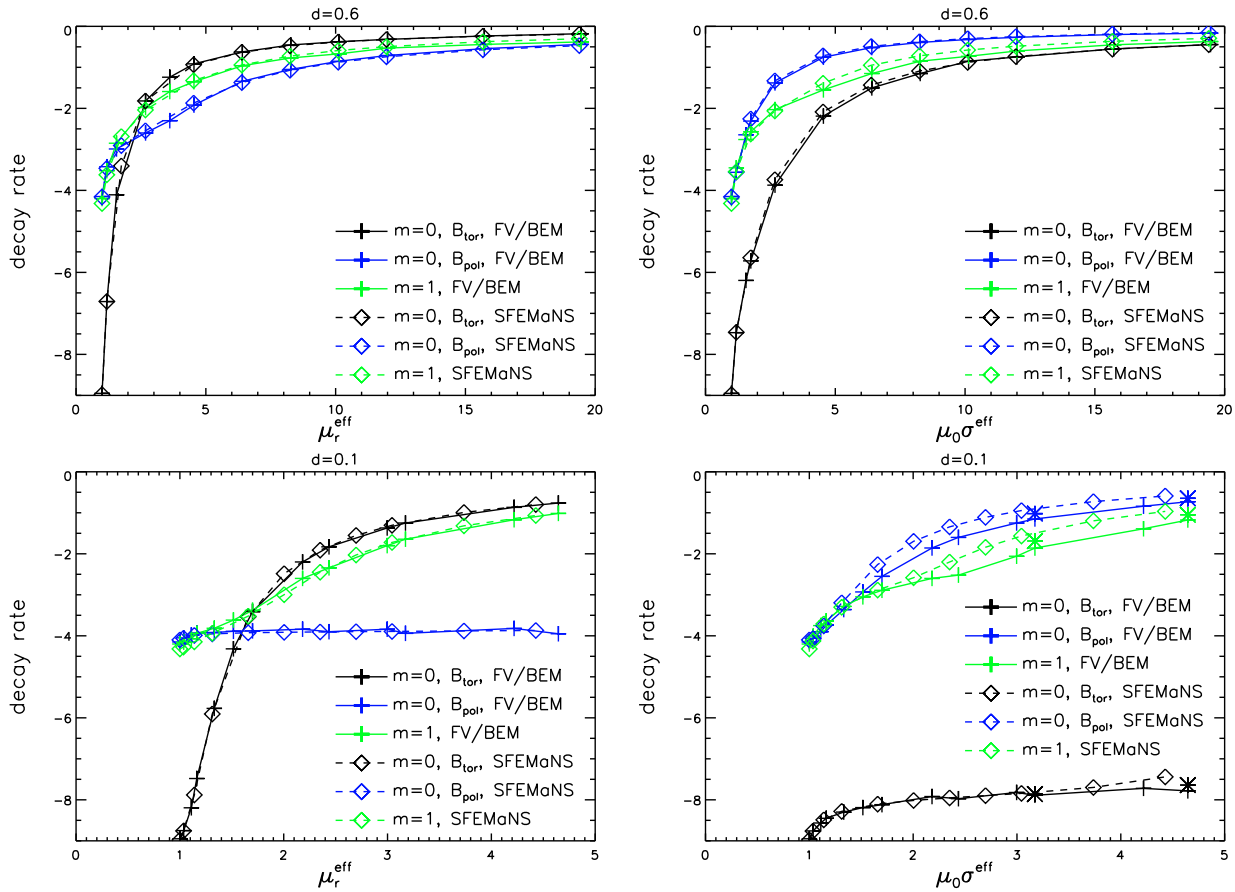


Figure 7. Decay rates with vacuum BC against μ_r^{eff} (left column) and against $\mu_0\sigma^{\text{eff}}$ (right column) for $d = 0.6$ (top row) and $d = 0.1$ (bottom row). The solid curves show the results obtained from the hybrid FV/BEM scheme and the dashed curves denote the results from the SFEMaNS scheme. The stars in the lower right panel present the results of a FV/BEM run with higher resolution demonstrating that the FV/BEM algorithm might approach the SFEMaNS data.

are available to resolve the vertical structure of the disk (namely 40 mesh points for SFEMaNS against 6 mesh points for FV/BEM). A more systematic discrepancy between both algorithms becomes obvious by means of the behavior of the decay time τ defined by the reciprocal value of the decay rate (see Fig. 8). For sufficient large μ_r^{eff} (respectively σ^{eff}), τ varies following a scaling law $\tau \propto c\mu_r^{\text{eff}}$ (respectively $\propto c\sigma^{\text{eff}}$) as reported in table 1. For increasing μ_r^{eff} the decay time of the ($m = 0$) toroidal mode slightly increases with decreasing d whereas the axisymmetric poloidal mode exhibits an opposite behavior. The variation of the decay time with σ^{eff} for the ($m = 0$) components (toroidal and poloidal) is the opposite to the ones with varying μ_r^{eff} . These variations suggest that the decay time scaling law is not only due to the ferromagnetic volume of the impellers but also to the geometric constraints associated with the jump conditions (2.3).

The evaluation of the discrepancies in the scaling behavior obtained by both numerical schemes remains difficult because this would require larger values for μ_r^{eff} and/or σ^{eff} which is not possible without significantly improving the numerical schemes. In particular for the thin disk case ($d = 0.1$) the achievable values for μ_r and/or σ are restricted to μ_r^{eff} (respectively $\mu_0\sigma^{\text{eff}}$) $\lesssim 5$ and, it is not obvious if the available data already belongs to the region that follows a linear scaling. In any case the absolute values for the decay rates obtained by both algorithms are close, giving confidence that the results imply a sufficient accurate description of the magnetic field behavior in the presence of non-heterogenous materials.

As already indicated by the marginal differences in the field pattern for both examined boundary conditions, we find no qualitative change in the behavior of the decay rates or decay times with vacuum boundary conditions or VTF boundary conditions (see Fig. 9). Although for small values of μ_r^{eff} and σ^{eff} the absolute values of the decay rates differ by 30% the scaling behavior of the decay time is nearly independent of the

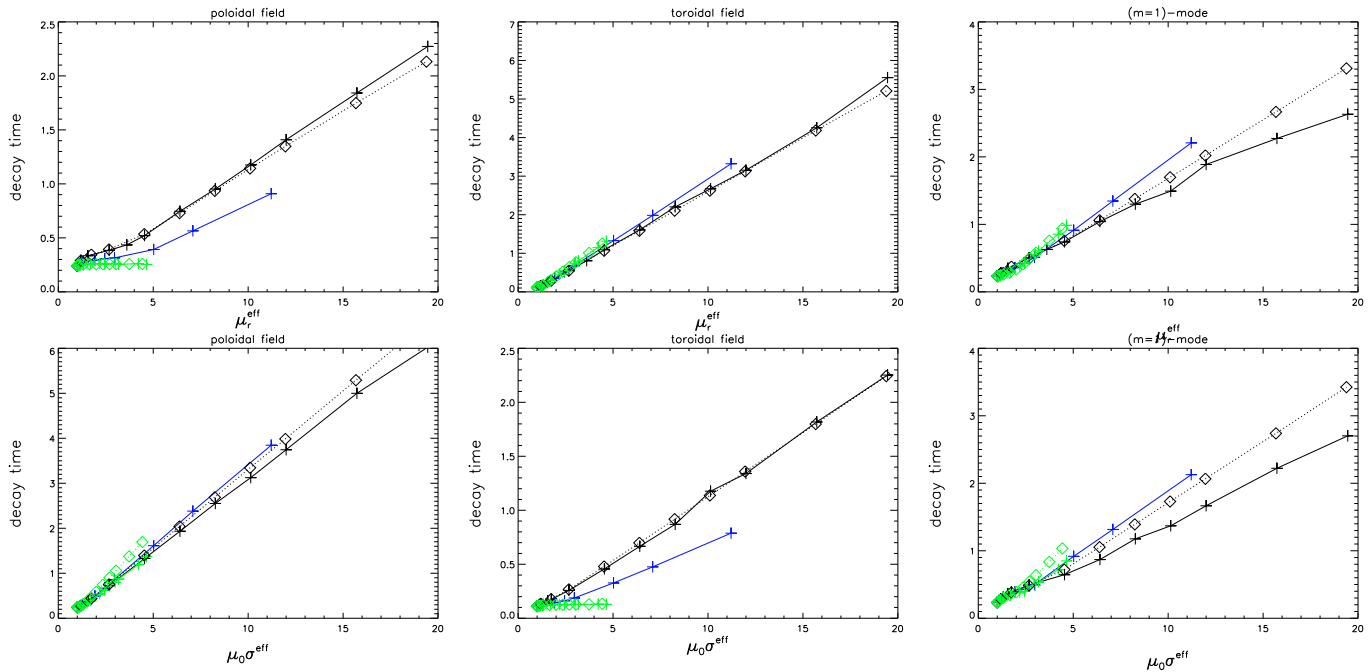


Figure 8. Ohmic decay. Decay times against μ_r^{eff} (top row) and against $\mu_0\sigma^{\text{eff}}$ (bottom row) for three disk thicknesses $d = 0.6, 0.3, 0.1$ (black, blue, green). The solid curves show the results obtained from the hybrid FV/BEM scheme and the dotted curves denote the results from the SFEMaNS scheme.

d	μ_r^{eff}			σ^{eff}			Algorithm
	0.6	0.3	0.1	0.6	0.3	0.1	
$\tau(B_{m=0}^{\text{tor}})$	0.29	0.32	0.33	0.12	0.07	0.00	FV/BEM
	0.28	–	0.34	0.12	–	0.00	SFEMaNS
$\tau(B_{m=0}^{\text{pol}})$	0.12	0.08	0.00	0.32	0.36	0.33	FV/BEM
	0.11	–	0.00	0.35	–	0.45	SFEMaNS
$\tau(B_{m=1})$	0.12	0.21	0.25	0.14	0.20	0.20	FV/BEM
	0.17	–	0.25	0.18	–	0.28	SFEMaNS

Table 1. Scaling coefficient c for the decay time as $\tau \propto c\mu_r^{\text{eff}}$ (respectively $c\mu_0\sigma^{\text{eff}}$) for different $m = 0$ and $m = 1$ modes as indicated (vacuum BC).

external boundary conditions (see Tab. 2). For increasing μ_r the influence of these boundary conditions is further reduced. Whereas the decay rates (for the thick disks) differ by approximately 30% for $\mu_r \lesssim 5$ there are nearly no differences in γ for higher values of the permeability. This behavior is less obvious in case of a high conductivity disk where the poloidal axisymmetric field exhibits differences in the decay rates of 15% even at the highest available conductivity (see Fig. 10). Note that the axisymmetric toroidal field behaves exactly in the same way for both kinds of boundary conditions because insulating boundary conditions and vanishing tangential field conditions are identical for the axisymmetric part of B_φ .

	μ_r^{eff}	σ^{eff}	
$\tau(B_{m=0}^{\text{tor}})$	0.29	0.12	FV/BEM VTF
	0.28	0.12	SFEMaNS VTF
$\tau(B_{m=0}^{\text{pol}})$	0.12	0.37	FV/BEM VTF
	0.10	0.42	SFEMaNS VTF
$\tau(B_{m=1})$	0.11	0.14	FV/BEM VTF
	0.17	0.19	SFEMaNS VTF

Table 2. Scaling coefficient c for the decay time as $\tau \propto c\mu_r^{\text{eff}}$ for thick disks ($d = 0.6$) and VTF boundary conditions.

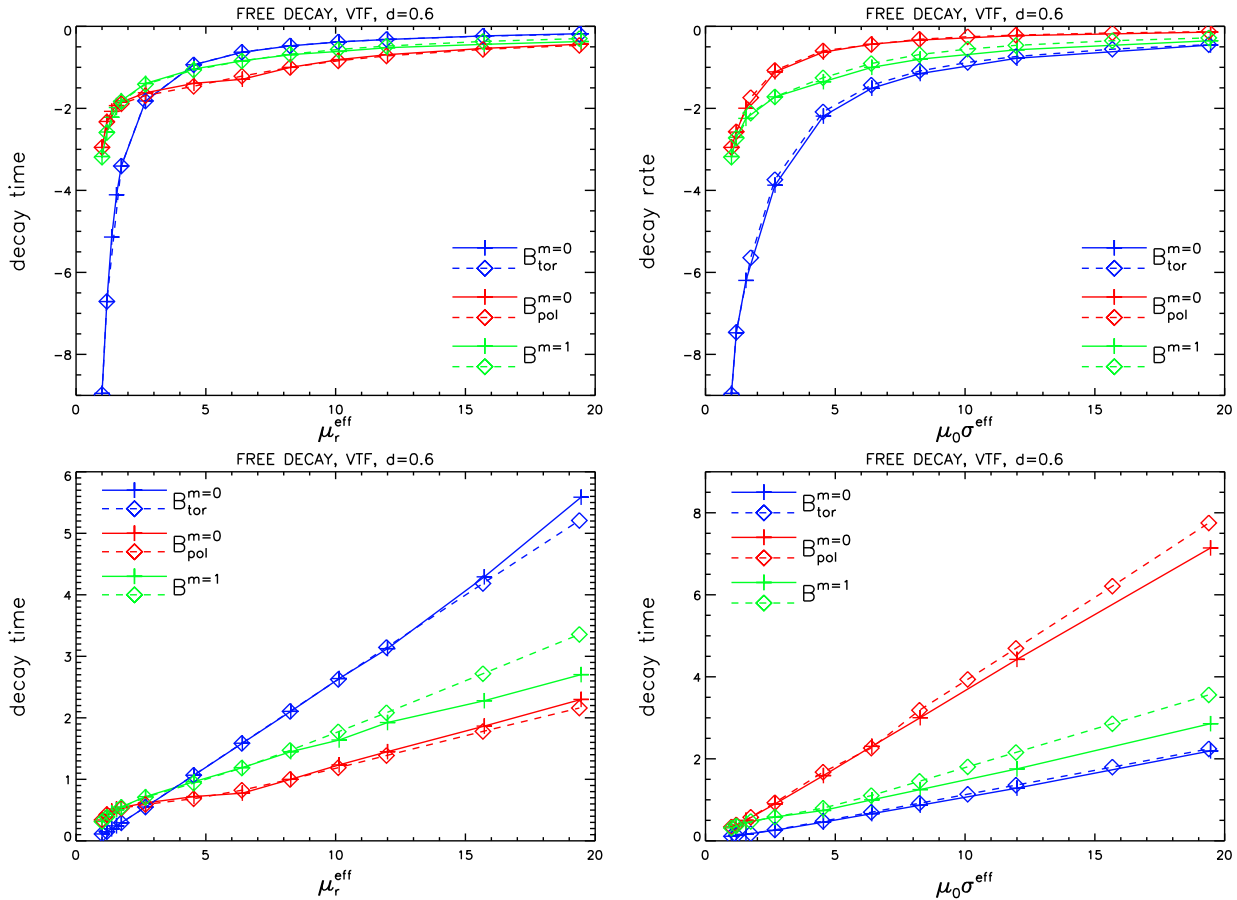


Figure 9. Decay rates and decay times against μ_r^{eff} (left column) and against $\mu_0 \sigma^{\text{eff}}$ (right column) for vanishing tangential fields boundary conditions. $d = 0.6$ The solid (dashed) curves denote the results from the FV/BEM (SFEMaNS) scheme.

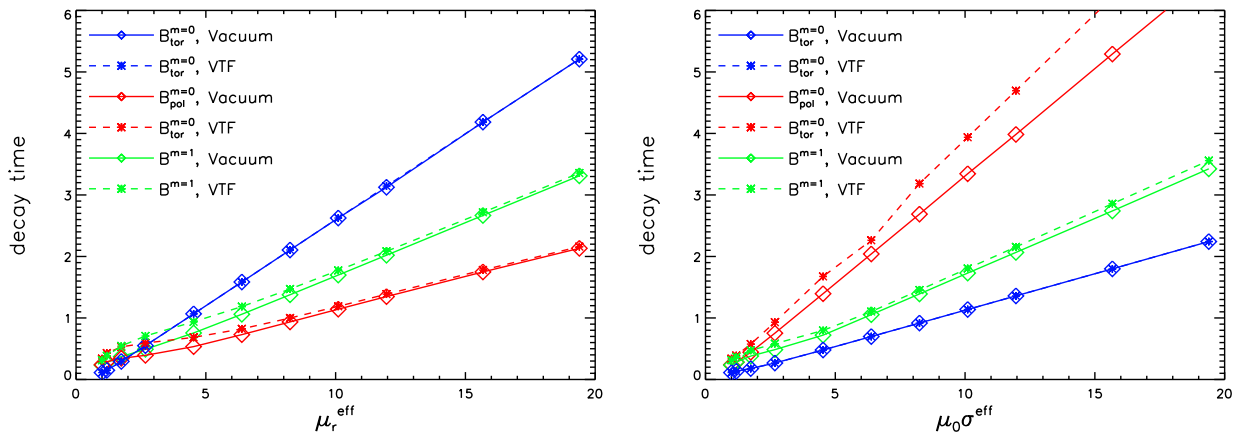


Figure 10. Comparison of boundary conditions. Decay times against μ_r^{eff} (left panel) and against $\mu_0 \sigma^{\text{eff}}$ (right panel) for vacuum BC (solid curves) and VTF boundary conditions (dashed curves). $d = 0.6$. All data results from the SFEMaNS scheme.

5 Kinematic Dynamo

In the following, the kinematic induction equation is solved numerically with $Rm > 0$ in order to examine if the behavior of the magnetic field obtained in the free decay is maintained when interaction with a mean flow is allowed. With reference to the VKS experiment we apply the so called MND-flow (Marié *et al.*

2006) given by

$$\begin{aligned} u_r(r, z) &= -(\pi/H) \cos(2\pi z/H) r(1-r)^2(1+2r), \\ u_\varphi(r, z) &= 4\epsilon r(1-r) \sin(\pi z/H), \\ u_z(r, z) &= (1-r)(1+r-5r^2) \sin(2\pi z/H), \end{aligned} \quad (5.1)$$

where $H = 1.8$ denotes the distance between both impeller disks and ϵ describes the relation between toroidal and poloidal component of the velocity (here, $\epsilon = 0.7259$ is chosen following previous work, e.g. Stefani *et al.* 2006). The flow magnitude is characterized by the magnetic Reynolds number which is defined as

$$\text{Rm} = \mu_0 \sigma U_{\max} R, \quad (5.2)$$

where U_{\max} is the maximum of the flow velocity and σ denotes the fluid conductivity. Figure 11 shows the structure of the velocity field where Eqs. (5.1) are only applied in the region between the two impellers. The flow active region with radius $R = 1$ (corresponding to 20.5 cm in the experiment) is surrounded by a layer of stagnant fluid with a thickness of $0.4R$ (the side layer) which significantly reduces Rm^c (Stefani *et al.* 2006). In the domain of the impellers a purely azimuthal velocity is assumed given by the

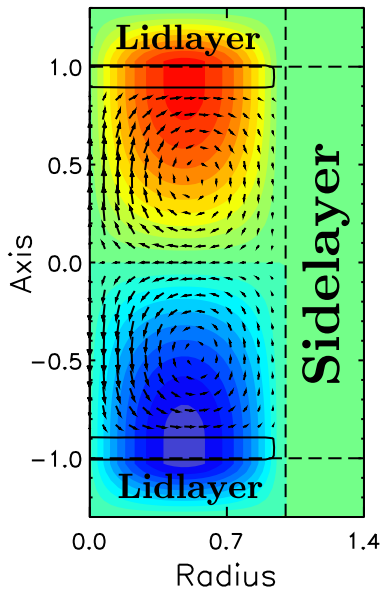


Figure 11. Structure of the prescribed axisymmetric velocity field. The color coded pattern represents the azimuthal velocity and the arrows show the poloidal velocity field. The black solid lines represent the shape of the impeller disk.

azimuthal velocity of the MND flow (Eq. 5.1) at $z = \pm H/2$. Behind each impeller disk a so called lid layer is added. Within these lid layers a purely rotating flow is assumed, modeled by a linear interpolation of the azimuthal velocity at the outer side of the impeller disk towards to zero at the end cap of the cylindrical domain. Similar to the simulations of free decay two disks are inserted into the computational domain (see solid black lines in Fig. 11). Here we limit our examinations to disks with a height $d = 0.1$. Note that the impellers are modeled only by the permeability and/or conductivity distribution and no particular flow boundary conditions are enforced on the (assumed) interface between impeller and fluid. This setup is comparable to the configuration in Giesecke *et al.* (2010b) except that the non axisymmetric permeability contribution representing the blade structure has been dropped in the present study.

Figure 12 shows the growth rates for the ($m = 1$) mode for different magnetic Reynolds numbers. Compared to the free decay, we obtain a remarkable distinct behavior of the growth rate if induction from a mean flow is added. A high permeability disk with $\text{Rm} > 0$ causes an enhancement of the ($m = 1$) mode

compared to the case $\mu_r = 1$. The shift of the growth rate increases with increasing Rm resulting in a non-negligible impact on the critical magnetic Reynolds number for the onset of dynamo action. In order to get insight in the experimental values necessary to get dynamo action, we have computed different thresholds for the ($m = 1$) mode: Rm^c is reduced from around 76 at $\mu_r = 1$ to Rm^c around 55 at $\mu_r = 100$. The behavior of Rm^c indicates a saturation around $Rm^c \approx 55$ for $\mu_r \gg 1$ which still lies above the experimental achievable value of approx 50. With respect to the Ohmic decay ($Rm = 0$) the ($m = 1$)-mode is clearly suppressed with increasing μ_r (see green curve in Fig. 12).

For a conducting disk we obtain a reduction of the ($m = 1$) growth rate. In both cases the ($m = 1$) decay rate remains independent of μ_r (respectively σ) for values exceeding approximately $\mu_r \approx 20$ (or $\mu_0\sigma \approx 20$). The critical magnetic Reynolds number has also been computed for a different set-up with

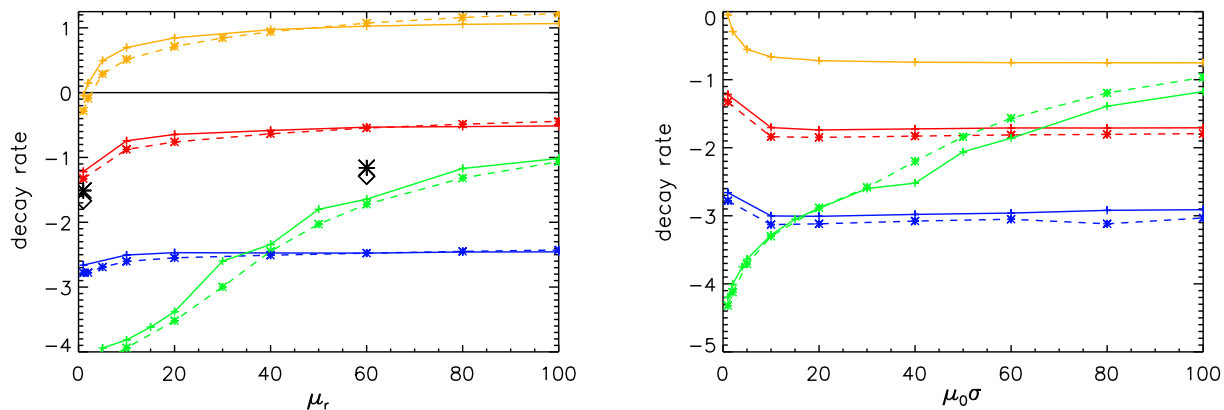


Figure 12. Growth rates for the MND flow driven dynamo against μ_r (left panel) and against $\mu_0\sigma$ (right panel). Solid curves denote data obtained from the FV/BEM scheme, dashed curves denote the results from the SFEMaNS scheme. The green, blue, red, yellow colors denote the cases $Rm = 0, 30, 50, 70$. The black stars in the left panel show the results for the SMND flow at $Rm = 50$ (see text) as reported in Tab. 3.

the fluid restricted to the bulk region : $0 \leq r \leq 1.4$, $-0.9 \leq z \leq 0.9$ with VTF conditions applied on the frontier of this region which results in $Rm^c = 39$. Note that this pseudo-vacuum set-up under-estimates the threshold by more than 30%. This confirms that a realistic description of the soft iron impellers is crucial to get correct estimates.

The robustness of the solutions suffers from the rather delicate dependence of the field behavior on the details of the flow distribution, in particular from the flow in the lid layers. Beside the well known dynamo killing influence of the lid flow (Stefani *et al.* 2006) this is also true for the radial flow in the vicinity of the inner side of the disks. A couple of simulations have been performed applying a slightly different velocity field where the radial component is smoothed at the transition between the bulk of the domain and the impeller disk (where $u_r = 0$). The resulting decay rates (black stars in the left panel of Fig. 12 and Tab. 3) exhibit slight differences in case of $\mu_r = 1$ and a more moderate enhancement of the ($m = 1$) - mode for $\mu_r = 60$.

$m = 1, Rm = 50$	$\mu_r = 1(\text{FV/BEM})$	$\mu_r = 1(\text{SFEMaNS})$	$\mu_r = 60(\text{FV/BEM})$	$\mu_r = 60(\text{SFEMaNS})$
MND	-1.218	-1.327	-0.550	-0.655
SMND	-1.51	-1.667	-1.16	-1.291

Table 3. Decay rate for $m = 1$ mode for 2 flows MND and a similar flow with slightly modified (smoothed) radial velocity component (SMND).

6 Conclusions

Although soft iron is strongly connected to magnetostatics, experimental dynamos have shown that this material may also find important applications in the field of magnetohydrodynamics. For instance, at least one of the two impellers of the Cadarache experiment must be made of soft iron in order to achieve dynamo action. This is an unexplained fact which suggests that one may wonder if the role of this material is only to lower the critical magnetic Reynolds number in the domain of experimental feasibility or if the dynamo mechanism is fundamentally different when the conducting medium is no longer homogenous. This issue may be faced in principle numerically. However, to face such problems with heterogenous domains, specific algorithms must be implemented and validated and this is the aim of the present study since analytical results are lacking. Our comparative runs of Ohmic decay problems proved in practice to be extremely useful to optimize both codes and to select some numerical coefficients occurring in the algorithms (such as in penalty terms).

The problems which have been successively presented above are standard in MHD, but we were forced to reduce the dimension of the parameter space to configurations more or less related to the Cadarache experiment, where the impellers may be treated as disks in a conducting flow bounded by a cylinder of a given aspect ratio. We have thus considered axisymmetric domains only (see Giesecke *et al.* (2010b) for non-axisymmetric cases), and azimuthal modes of low order ($m = 0$ and 1).

We have first studied Ohmic decay problems, with disk impellers of various thicknesses to investigate scaling laws and the impact of the spatial resolution. Internal assemblies of high permeability material within the fluid container are different from the problem of an enhanced, but homogenous fluid permeability because of inner boundary conditions for the magnetic field (in case of high permeability material), respectively for the electric field/current (in case of conductivity jumps). In the free decay problem with thin high permeability disks a selective enhancement of the axisymmetric toroidal field and the ($m = 1$) mode is observed whereas the axisymmetric poloidal field component is preferred in case of high conductive disks.

We have also shown that pseudo-vacuum boundary conditions, which are easier to implement on the cylinder walls than the jump conditions on the impellers, have only a slight influence on the decay rates. The impact of the outer container boundaries on the field behavior is limited to a shift of the decay/growth rates. This is surprising, insofar as pseudo vacuum boundary conditions resemble the conditions that correspond to an external material with infinite permeability. Nevertheless, the presence of high permeability/conductivity disks within the liquid occlude the influence of outer boundary conditions, and the simplifying approach applying vanishing tangential field conditions at the end caps of the cylinder in order to mimic the effects of the high permeability disks in the VKS experiment is not sufficient to describe the correct field behavior. The consideration of lid layers and disks with (large but finite) permeability remains indispensable in order to obtain the influence of the material properties on growth rates as well as on the field geometry.

For completeness, we have also considered conductivity domains. From the experimental point of view the utilization of disks with a conductivity that is 100 times larger than the conductivity of liquid sodium remains purely academic. Nevertheless, the simulations show a crucial difference between heterogeneous permeabilities and conductivities: even if these two quantities may appear in the definition of an effective Reynolds number $Rm^{\text{eff}} = \mu_0 \mu_r^{\text{eff}} \sigma^{\text{eff}} UL$, they do not play the same role and they select different geometries of the dominant decaying mode. It is not only a change of magnetic diffusivity that matters.

We considered then kinematic dynamo action, using analytically defined flows in accordance with the setting of the VKS mean flow. Since these flows are axisymmetric, the azimuthal modes are decoupled. The most important is the ($m = 1$) mode which will be excited eventually through dynamo action. We have shown that our codes give comparable growth rates for this mode. We have examined also the growth rate of the ($m = 0$) magnetic field in presence of soft iron impellers and the axisymmetric MND flow. Since convergence of results is not achieved in all the cases considered, this comparative study is still in progress and it has thus not been included in the present paper. We recall that the main surprise of the Cadarache experiment was perhaps the occurrence of the mode ($m = 0$), which pointed out the possible role of the non-axisymmetric flow fluctuations. Non-axisymmetric velocity contributions might be considered in terms

of an α -effect as it has been proposed in Pétrélis *et al.* (2007) and Laguerre *et al.* (2008a,b). Preliminary examinations applying simple α -distributions are presented in Giesecke *et al.* (2010a) and Giesecke *et al.* (2010b). However, there is still a lack of knowledge on the details and physical justification on a precise α -distribution which requires a non-linear hydrodynamic code. The questions related to this empirical fact represent a main issue of the experimental and numerical approaches of the fluid dynamo problem and deserve a dedicated study. So far our model is not capable to explain the main features of the VKS experiment, which are the dominating axisymmetric field mode and the surprising low critical magnetic Reynolds number of $Rm \approx 32$. However, our results give a hint why the ($m = 1$) mode remains absent in the experiment. Dynamo action may occur when coupling terms between the magnetic field components are present and antidynamo theorems are derived when such terms are lacking: this is in particular the case for the ($m = 0$) mode with an axisymmetric flow (Cowling's theorem). Conversely, a source term on this mode appears when the flow axisymmetry is broken. Although the relative amplitude of this source cannot be discussed here, we note that the decay time of the ($m = 0$) toroidal mode become the smallest when the effective permeability is high enough (see for example Fig. 7). It may thus appears as the dominant mode of the dynamo, as it seems to be observed in the VKS experiment. Otherwise stated, the impact of soft-iron impellers on the critical magnetic Reynolds number of the ($m = 1$)-mode could be rather low (decrease from ~ 76 to ~ 55 in the MND case) and could remain unobservable, while it could be strong for the ($m = 0$) mode (down to 32 in the VKS geometry) when conjugated to a slight departure from flow axisymmetry. Numerical evidences of this picture are growing.

Acknowledgments

Financial support from Deutsche Forschungsgemeinschaft (DFG) in frame of the Collaborative Research Center (SFB) 609 is gratefully acknowledged and from European Commission under contract 028679. The computations using SFEMaNS were carried out on the IBM SP6 computer of Institut du Développement et des Ressources en Informatique Scientifique (IDRIS) (project # 0254).

REFERENCES

- Bonito, A., Guermond, J.L. and Luddens, F., Approximation of the Eigenvalue Problem for Time Harmonic Maxwell System by Continuous Lagrange Finite Elements. *Math. Comp.* 2010 Under review.
- Busse, F.H. and Wicht, J., A simple dynamo caused by conductivity variations. *Geophys. Astrophys. Fluid Dyn.* 1992, **64**, 135–144.
- Costabel, M., A coercive bilinear form for Maxwell's equations. *J. Math. Anal. Appl.* 1991, **157**, 527–541.
- Dobler, W., Frick, P. and Stepanov, R., Screw dynamo in a time-dependent pipe flow. *Phys. Rev. E* 2003, **67**, 056309–+.
- Frick, P., Khripchenko, S., Denisov, S., Sokoloff, D. and Pinton, J.F., Effective magnetic permeability of a turbulent fluid with macroferroparticles. *Eur. Phys. J. B* 2002, **25**, 399–402.
- Giesecke, A., Stefani, F. and Gerbeth, G., Kinematic simulations of dynamo action with a hybrid boundary-element/finite-volume method. *Magnetohydrodynamics* 2008, **44**, 237–252.
- Giesecke, A., Nore, C., Plunian, F., Laguerre, R., Ribeiro, A., Stefani, F., Gerbeth, G., Léorat, J. and Guermond, J., Generation of axisymmetric modes in cylindrical kinematic mean-field dynamos of VKS type. *Geophys. Astrophys. Fluid Dyn.* 2010a, **104**, 249–271.
- Giesecke, A., Stefani, F. and Gerbeth, G., Role of Soft-Iron Impellers on the Mode Selection in the von Kármán–Sodium Dynamo Experiment. *Phys. Rev. Lett.* 2010b, **104**, 044503.
- Guermond, J.L., Laguerre, R., Léorat, J. and Nore, Nonlinear magnetohydrodynamics in axisymmetric heterogeneous domains using a Fourier/Finite Element technique and an Interior Penalty Method. *J. Comput. Phys.* 2009, **228**, 2739–2757.
- Guermond, J.L., Laguerre, R., Léorat, J. and Nore, C., An interior penalty Galerkin method for the MHD equations in heterogeneous domains. *J. Comput. Phys.* 2007, **221**, 349–369.

- Haber, E. and Ascher, U.M., Fast Finite Volume Simulation of 3d electromagnetic problems with highly discontinuous coefficients. *SIAM J. Sci. Comput.* 2001, **22**, 1943–1961.
- Iskakov, A.B. and Dormy, E., On magnetic boundary conditions for non-spectral dynamo simulations. *Geophys. Astrophys. Fluid Dyn.* 2005, **99**, 481–492.
- Iskakov, A.B., Descombes, S. and Dormy, E., An integro-differential formulation for magnetic induction in bounded domains: boundary element-finite volume method. *J. Comp. Phys.* 2004, **197**, 540–554.
- Jackson, J.D., *Classical electrodynamics*, 1975 (New York: Wiley, 1975, 2nd ed.).
- Laguerre, R., Nore, C., Ribeiro, A., Léorat, J., Guermond, J. and Plunian, F., Impact of Impellers on the Axisymmetric Magnetic Mode in the VKS2 Dynamo Experiment. *Physical Review Letters* 2008a, **101**, 104501–+.
- Laguerre, R., Nore, C., Ribeiro, A., Léorat, J., Guermond, J. and Plunian, F., Erratum: Impact of Impellers on the Axisymmetric Magnetic Mode in the VKS2 Dynamo Experiment [Phys. Rev. Lett. 101, 104501 (2008)]. *Phys. Rev. Lett.* 2008b, **101**, 219902–+.
- Lowes, F.J. and Wilkinson, I., Geomagnetic Dynamo: A Laboratory Model. *Nature* 1963, **198**, 1158–1160.
- Lowes, F.J. and Wilkinson, I., Geomagnetic Dynamo: An Improved Laboratory Model. *Nature* 1968, **219**, 717–718.
- Marié, L., Normand, C. and Daviaud, F., Galerkin analysis of kinematic dynamos in the von Kármán geometry. *Phys. Fluids* 2006, **18**, 017102–+.
- Monchaux *et al.*, R., Generation of a Magnetic Field by Dynamo Action in a Turbulent Flow of Liquid Sodium. *Phys. Rev. Lett.* 2007, **98**, 044502.
- Pétrélis, F., Mordant, N. and Fauve, S., On the magnetic fields generated by experimental dynamos. *Geophys. Astrophys. Fluid Dyn.* 2007, **101**, 289–323.
- Stefani, F., Xu, M., Gerbeth, G., Ravelet, F., Chiffaudel, A., Daviaud, F. and Leorat, J., Ambivalent effects of added layers on steady kinematic dynamos in cylindrical geometry: application to the VKS experiment. *Eur. J. Mech. B* 2006, **25**, 894–908.
- Stone, J.M. and Norman, M.L., ZEUS-2D: A radiation magnetohydrodynamics code for astrophysical flows in two space dimensions. I - The hydrodynamic algorithms and tests.. *Astrophys. J. Supp.* 1992a, **80**, 753–790.
- Stone, J.M. and Norman, M.L., ZEUS-2D: A Radiation Magnetohydrodynamics Code for Astrophysical Flows in Two Space Dimensions. II. The Magnetohydrodynamic Algorithms and Tests. *Astrophys. J. Supp.* 1992b, **80**, 791–+.
- Verhille, G., Plihon, N., Bourgoïn, M., Odier, P. and Pinton, J., Induction in a von Kármán flow driven by ferromagnetic impellers. *New J. Phys.* 2010, **12**, 033006–+.
- Ziegler, U., A three-dimensional Cartesian adaptive mesh code for compressible magnetohydrodynamics. *Comp. Phys. Comm.* 1999, **116**, 65–77.